Available online at www.sciencedirect.com
SCIENCE DIRECT®
Combustion and Flame 141 (2005) 1–21
Combustion and Flame
www.elsevier.com/locate/combustflame

Measured properties of turbulent premixed flames for model assessment, including burning velocities, stretch rates, and surface densities

Sergei A. Filatyev [a], James F. Driscoll [a,*], Campbell D. Carter [b], Jeffrey M. Donbar [b]

[a] *Department of Aerospace Engineering, University of Michigan, Ann Arbor, MI 48109, USA*
[b] *Air Force Research Laboratory AFRL/PRAS, Wright–Patterson AFB, OH 45433, USA*

Received 20 September 2003; received in revised form 4 May 2004; accepted 20 July 2004

Available online 25 September 2004

Abstract

Several previously unreported properties of turbulent premixed flames were measured because they are especially useful for the future assessment of direct numerical simulations and models. These new properties include local stretch rates, a wrinkling parameter, the degree of flamelet extinction, and the reaction layer thickness, which were quantified using simultaneous CH planar laser-induced fluorescence/particle image velocimetry (CH PLIF-PIV) diagnostics. Other reported properties that are useful for model assessment are flame surface density (Σ) and global consumption speed, which is one type of turbulent burning velocity. Also measured was the Meneveau–Poinsot stretch efficiency function (Γ_K), which plays a central role in the coherent flamelet model. Some images of the flame–eddy interactions show how eddies exert strain and how flamelets "merge." A highly wrinkled (corrugated) flame with well-defined boundary conditions was stabilized on a large two-dimensional slot Bunsen burner. It was found that the turbulent burning velocity of Bunsen flames depends on the mean velocity $\bar{U}$, which was varied independently of turbulence intensity. It is concluded that conventional relations for the turbulent burning velocity of Bunsen flames are inadequate because they should include two additional parameters: mean velocity $\bar{U}$ and burner width W. These parameters affect the residence times of the flame–eddy interactions. A scaling analysis is presented to explain the observed trends. It indicates that if the burner width is sufficiently large, the long flame will experience significant flamelet merging, which is one factor leading to the "bending" (nonlinear behavior) of the burning velocity curve. Images of CH layers show that flame surface area is lost by flamelet merging, but is not lost due to local extinction, as no extinction was observed. The stretch efficiency function increases with increasing integral scale, indicating that large eddies are more efficient in exerting flame stretch than small eddies.

Keywords: Burning velocity; Premixed turbulent flames; Stretch

* Corresponding author. Fax: +1(734)763-0578.
E-mail address: jamesfd@umich.edu (J.F. Driscoll).

0010-2180/$ – see front matter
doi:10.1016/j.combustflame.2004.07.010

Nomenclature

$\bar{A}_F$	frontal area of flame brush (Eq. (5a))
$\bar{c}$	mean reactedness
H	height of Bunsen flame
I_0	stretch factor (Eq. (1))
K	stretch rate (Eq. (9))
Ka	Karlovitz number
L	length of burner (Fig. 1)
$\dot{m}_R$	mass flow rate of reactants
$\bar{M}$	flamelet merging term (Eq. (2))
$\tilde{m}$	$\bar{M}/\Sigma$
Ma	Markstein number
$\bar{P}$	perimeter of time-averaged flame position in laser sheet (Fig. 1)
P_T	perimeter of wrinkled flame surface, averaged over 70 images
$\bar{Q}$	flamelet quenching term (Eq. (2))
S_{L0}	unstretched laminar burning velocity = 0.38 mls
S_T	local consumption speed
$\bar{S}_T$	turbulent burning velocity defined as a global consumption speed (Eq. (5c))
$\bar{U}$	streamwise velocity averaged over burner exit $= \dot{m}_R/(\rho_R L W)$
$\tilde{U}$	Favre-averaged streamwise velocity
$U_{CL,0}$	mean velocity at origin (Fig. 1)
u'	root-mean-squared velocity fluctuations
W	burner width (Fig. 1)
x	streamwise coordinate (Fig. 1)
y	lateral coordinate (Fig. 1)
α_0	thermal diffusivity of reactants at 296 K, 0.18 cm^2
δ_{CH}	CH reaction layer thickness
δ_{L0}	unstretched laminar flame thickness, $= 7.4\alpha_{L0}/S_{L0} = 0.35$ mls
δ_T	turbulent brush thickness
η	coordinate normal to flame brush
Γ_K	stretch efficiency function (Eq. (3))
ν_T	turbulent diffusivity
ℓ	integral scale of turbulence
Σ	flame surface density
Ω	wrinkling factor (Eq. (22))

1. Introduction

One goal of this work was to quantify several properties of turbulent premixed flames that have not been quantified before and are especially useful for the assessment of direct numerical simulations (DNS) and models. It was decided to select a flame that is in the "corrugated flamelet regime" and use simultaneous CH planar laser-induced fluorescence/particle image velocimetry (CH PLIF/PIV) diagnostics, which previously had been applied only to nonpremixed combustion. These diagnostics allow one to identify the thin wrinkled reaction zone (where CH exists) and the nearby velocity field. Properties that were measured include local stretch rates, a wrinkling parameter, the degree of flamelet extinction, reaction layer thicknesses, flame surface density (Σ), and global consumption speed, which is one type of turbulent burning velocity that is described below.

Recently, Bell et al. [1] obtained impressive DNS results for a turbulent premixed flame in three dimensions with complex chemistry and an adaptive grid resolution of 62.5 μm. However, to determine if the grid resolution is adequate and if the boundary conditions were handled properly, comparisons of DNS results with measurements are required. If a modeling approach is employed (instead of DNS), two promising models are the coherent flamelet model (CFM), which is based on the Reynolds-averaged Navier–Stokes and flame surface density equations, and the large eddy simulation with a flame surface density subgrid model (LES-FSD). The CFM has been used to simulate Bunsen flames, V-flames, spherical flames, and planar flames by Prasad and Gore [2], Veynante et al. [3], Baritaud et al. [4], and Duclos et al. [5], respectively. Alternatively, the LES-FSD model [6–9] has been applied to bluff-body flames by Knikker et al. [8] and Weller et al. [9].

To assess DNS, LES, or CFM results, it is important that the following three physical mechanisms are correctly simulated.

(1) The turbulent burning velocity (S_T) is enhanced by the increase in surface area of the wrinkled reaction zone, which can be quantified by the flame surface density (Σ).
(2) This increase in surface area of the reaction zone is caused by the stretch rate (K) that is induced by local velocity gradients and flame curvature.
(3) The stretch rate (K) of the flame is caused by vortical motions associated with turbulent eddies.

To determine if these mechanisms are simulated correctly, measurements of the quantities S_T, K, and Σ are of central importance. The relationship between these three quantities is shown by equations that were derived by Bray [10], Candel and Poinsot [11], and

Meneveau and Poinsot [12]:

$$S_T = S_{L0} I_0 \int_{-\infty}^{\infty} \Sigma \, d\eta, \tag{1}$$

$$\tilde{U}\frac{\partial \Sigma}{\partial x} + \tilde{V}\frac{\partial \Sigma}{\partial y} = \nu_T \frac{\partial^2 \Sigma}{\partial y^2} + \bar{K}\Sigma - \bar{Q} - \bar{M}, \tag{2}$$

$$\bar{K} = (u'/\ell)\Gamma_K. \tag{3}$$

Eq. (1) summarizes physical mechanism (1): the turbulent burning velocity is proportional to the wrinkled flame area, which is an idea that was proposed by Damkohler [13,14]. In Eq. (1) the flame surface density Σ is the average amount of flame surface area per unit volume, and η is the coordinate that is normal to the flame brush. The integral of $\Sigma \, d\eta$ has been shown [1] to equal the ratio A_T/A_L, where A_T is the wrinkled flame area and A_L is the flame area if there was no wrinkling. I_0 is a stretch factor, which has been shown [15] to be 1–0.28 $Ma\,Ka$; thus, I_0 is approximately 1.0 if the fuel–air ratio is chosen to yield a Markstein number that is sufficiently small, as was done in the present work. Eq. (2) summarizes physical mechanism (2): the increase in flame area is due to the mean stretch rate ($\bar{K}$), as well as the quantities $\bar{Q}$ and $\bar{M}$, which quantify the flamelet quenching and merging rates, respectively. Eq. (3) defines the Meneveau–Poinsot stretch efficiency function Γ_K that relates the mean stretch rate $\bar{K}$ to the rms velocity fluctuations u' and the integral scale ℓ [12]. Prior to the present study Γ_K could be estimated only from computational and experimental studies of a laminar flame interacting with a single vortex. The preferred way to determine Γ_K is to measure the stretch rate within turbulent flames, using the methods described below.

2. Categories of premixed flames

The decision was made to study a large Bunsen flame, which has been labeled an "envelope flame" by Cheng and Shepherd [16] because all of the reactants must pass through the flame. Other categories [16] are "oblique (rod-stabilized) flames" which have been documented by Knaus and Gouldin [17], "unattached" (low-swirl flames and counterflow flames [16]), spherical expanding flames, and shear-dominated (jetlike) premixed flames [18]. For each category the wrinkling process and the boundary conditions are different. Thus, the formula for the burning velocity for one category is expected to differ from that for another category. The formula should include a few category-specific parameters such as burner width (W) and mean velocity ($\bar{U}$). Experimental evidence indicates that there is no turbulent flame that is truly universal and category-independent. Therefore it is recommended that in any attempt to collapse values of turbulent burning velocity to a set of curves, only data from one category be considered. This implies that there will be a different plot of the burning velocity correlation for each category.

For example, two parameters that control Bunsen flames are the mean velocity and burner width, both of which affect the height of the flame. Taller flames become more wrinkled than short flames because it is observed that wrinkling increases with distance from the attachment point. Thus it can be expected that for Bunsen flames, a burning velocity correlation would depend on

$$\frac{\bar{S}_T}{S_{L0}} = fcn\left(\frac{u'}{S_{L0}}, \frac{\ell}{\delta_{L0}}, Ma, \frac{\bar{U}}{S_{L0}}, \frac{W}{\delta_{L0}}\right), \tag{4}$$

where Ma is the Markstein number for given fuel type and equivalence ratio. Ma has been shown to affect burning velocity even for very high Reynolds conditions [18]. The unstretched laminar flame thickness (δ_{L0}) is defined as the temperature difference across a laminar flame divided by the maximum temperature gradient; this distance is 7.4 (α_{L0}/S_{L0}) based on the measurements of Bechtel et al. [19]. For spherical flames the correlation would differ from Eq. (4) because $\bar{U}$ and W are not relevant parameters; instead, the degree of wrinkling and the propagation speed of a spherical flame depend on a different parameter: the total time during which the flame is exposed to the turbulence. The best approach is to identify the category-dependent parameters and then create a separate database and correlation of data for each category.

3. Experimental arrangement

The relatively large two-dimensional slot Bunsen burner shown in Fig. 1 was operated under the conditions listed in Table 1. One advantage of Bunsen geometry is that all of the reactants pass through the flame so the mass flow rate of the reactants that are consumed is known. The large burner width (W) of 25.4 mm creates a tall flame with a height exceeding 100 mm; this allows the flame to become highly wrinkled, so it provides a good test of the ability of a model to predict the correct degree of wrinkling.

The rectangular central burner in Fig. 1 contains a turbulence-producing grid, and this central burner is surrounded by two outer burners; all three burners have the exit dimensions $W = 25.4$ mm and $L = 50.8$ mm. Each outer burner contains a short grid-stabilized flames to provide a stream of products that have the same axial velocity as the products produced by the central flame. This eliminates any interaction

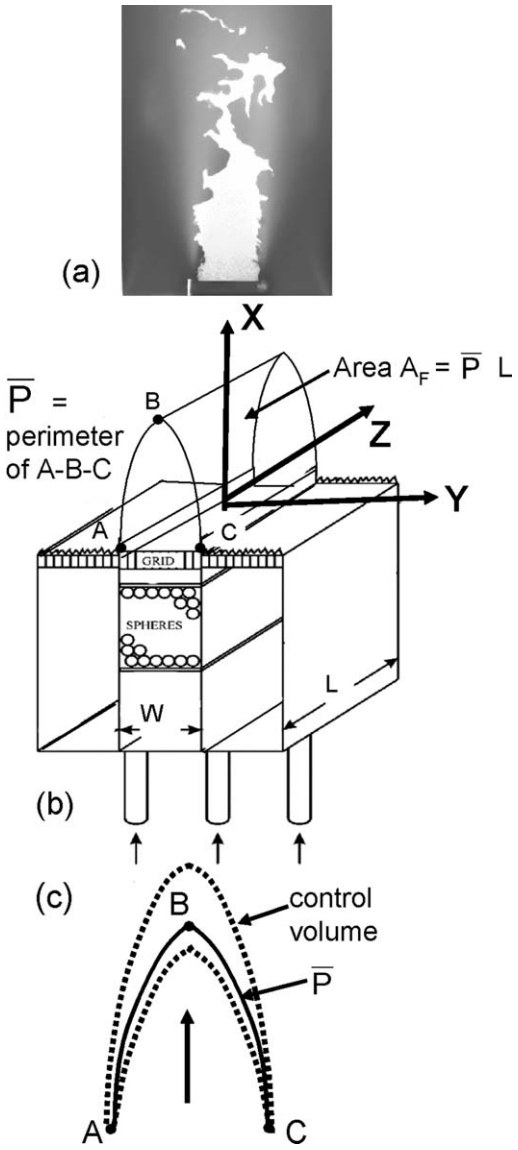

Fig. 1. The 2D slot Bunsen flame (a) and burner (b). Width W is 25.4 mm; length L is 50.8 mm. Two outer burners eliminate shear layers. $\bar{P}$ is the perimeter of the smooth curve from A to B to C, obtained by overlapping 70 images. Stoichiometric methane–air was used for all conditions. (c) Control volume considered.

between the central flame and shear layers that are associated with the interface between products and the surrounding room air. Therefore all of the flame wrinkling is due to the grid-generated turbulence. The reactants were stoichiometric methane and air, metered by mass flow controllers, for all cases and for all three burners. The pressure was 1 atm, the reactants entered at 296 K, S_{L0} is 38 cm/s, the unstretched laminar flame thickness δ_{L0} ($= 7.4\alpha_{L0}/S_{L0}$) [19] was 0.35 mm, and the Markstein number was 0.95 [20]. The turbulence intensity was varied by replacing the central burner with an identical burner that contained a different grid or a different layer of metal spheres. Table 1 shows the values of rms velocity fluctuations u' and mean velocity $U_{CL,0}$, which were measured with a laser velocimeter on the burner centerline just above the burner exit. The grid that imparted the lowest turbulence level was denoted the 5% burner; $u'/U_{CL,0}$ varied from 4 to 7% for different values of $\bar{U}$, but the average value was 5%. The other two burners were denoted the 10 and 20% burners, respectively. The spatially averaged burner exit velocity ($\bar{U}$) is defined as the measured mass flow rates of reactants provided to the central burner divided by the burner exit area and reactant density. Values of $\bar{U}$ were set at 3, 5, 8, and 12 m/s for cases 3, 5, 8, and 12, respectively. The integral scale ℓ at the burner exit was determined in the standard way from PIV data by computing the spatial correlation $\overline{u'(x)u'(x+\Delta x)}/\overline{u'^2}$ and integrating over all Δx where x is the vertical streamwidth coordinate. Integral scales varied from 3.1 to 12.8 mm and are listed in Table 1. For a typical condition (case 8c), the turbulence Reynolds number $u'\ell/\nu$ was 990, and the Karlovitz number based on the integral scale $(u'/\ell)/(S_{L0}^2/\alpha_0)$ was 0.020. Bray and Cant [15] showed that I_0 in Eq. (1) is 1–0.28 $Ka\,Ma$; thus I_0 has a value of 0.994.

To determine if any of the reactants can avoid passing through the flame, which is undesirable, oil drops were added to the reactants and were illuminated by a laser light sheet and no oil drops were observed to pass out the end planes (the plane in which points A, B, and C are located in Fig. 1). Also, no oil drops were observed anywhere in the product gases. Thus it is concluded that essentially none of the reactants can bypass the flame sheet. It also was determined that the mean flow field is two-dimensional and does not vary in the z direction (shown in Fig. 1) over the region $z = \pm 12.5$ mm, as shown in Appendix A. There were some edge effects of the end planes ($z = +25$ mm and $z = -25$ mm) but all measurements were made in the x–y plane ($z = 0$), which is far from the edges, so edge effects are not significant.

The simultaneous CH PLIF-PIV system is described in Appendix A and in Refs. [21–23], however many updates to the PIV system have been made; it is located at Wright–Patterson AFB. A 35 × 35-mm region was imaged at three different heights above the burner. The spatial resolution of the CH PLIF system was 0.2 mm, which equals the PLIF laser sheet thickness and the size of the 3 × 3-pixel region in the field of view over which the PLIF signal was averaged. The spatial resolution of the PIV system was set by the 0.27 mm interrogating box size (16 × 16 pixels) and the use of 50% overlap during PIV data reduction, and the size of the PIV interrogation box used.

Table 1
Properties of the 12 turbulent premixed flame cases[a]

Case	$\bar{U}$ (m/s)	$U_{CL,0}$ (m/s)	$\frac{u'}{U_{CL,0}}$	$\frac{u'}{S_{L0}}$	Integral scale, ℓ (mm)	Taylor scale, λ_T (mm)	Kolmogorov scale, λ_K (mm)
3a	3.0	2.7	0.04	0.28	–	–	–
3b	3.0	2.7	0.10	0.69	5.2	0.5	0.2
3c	3.0	3.4	0.24	2.14	3.1	0.2	0.07
5a	5.0	4.7	0.05	0.68	–	–	–
5b	5.0	4.4	0.10	1.12	–	–	–
5c	5.0	5.9	0.23	3.57	–	–	–
8a	8.0	7.3	0.05	1.00	–	–	–
8b	8.0	6.5	0.11	1.88	12.8	0.5	0.1
8c	8.0	8.5	0.20	4.47	8.7	0.3	0.05
12a	12.0	11.0	0.07	2.17	–	–	–
12b	12.0	11.4	0.16	4.80	–	–	–
12c	12.0	13.0	0.25	8.55	–	–	–

[a] $\bar{U}$ is the mean velocity that is spatially averaged over the burner exit; it is the mass flow rate of reactants divided by the burner exit area and the reactant density. $U_{CL,0}$ and u' were measured at the origin using laser velocimetry. S_{L0} is 0.38 m/s, δ_{L0} is 0.35 mm, burner width (W) is 25.4 mm, and $Ma = 0.95$.

4. Definition of the turbulent burning velocity: the global consumption speed ($\bar{S}_T$)

There is no single accepted definition of turbulent burning velocity; instead, four different velocities have been used in previous studies. These are the local and global displacement speeds (S_d and $\bar{S}_d$) and the local and global consumption speeds (S_T and $\bar{S}_T$). Each represents an acceptable way to characterize turbulent burning velocity, providing that one consistently uses the same definition when comparisons are made. Local displacement speed S_d is the relative velocity between some contour (such as $\bar{c} = 0.5$) and the gas velocity at some defined distance ahead of the flame; it is difficult to measure in Bunsen and V-flames because these contours are oblique to the incoming flow [24]. Measurements of the local consumption speed [25,26] require the measurement of mass fluxes, including the correlation $\overline{\rho' u'}$, on all boundaries of a small control volume.

In the present study, it was decided to measure the global consumption speed ($\bar{S}_T$). If we consider any wrinkled turbulent wave, the speed of the entire wave is the speed of the smooth surface that represents the time-averaged position of the wave. This time-averaged wave position is identified by the smooth curve A–B–C in Fig. 1b. The frontal area of the time-averaged flame position ($\bar{A}_F$) is defined as the perimeter ($\bar{P}$) of the smooth curve A–B–C multiplied by the length L shown in Fig. 1; thus,

$$\bar{A}_F = \bar{P} \cdot L. \tag{5a}$$

Now consider the control volume shown in Fig. 1c, which encloses the entire flame. The mass per second of reactants that enter through the upstream boundary of the control volume must equal the known mass flow rate provided to the burner ($\dot{m}_R$), so conservation of mass requires that

$$\dot{m}_R = \rho_R \bar{S}_T \bar{A}_F. \tag{5b}$$

The quantity ρ_R is the known density of the stoichiometric methane–air mixture at 296 K, 1 atm. It is appropriate to use ρ_R in Eq. (5b) since it is the density of the unburned gas through which the wave is propagating. $\bar{S}_T$ represents the global consumption speed because it is proportional to the total mass per second of reactants consumed. Eq. (5b) is rearranged to yield

$$\bar{S}_T = \dot{m}_R / (\rho_R \bar{A}_F). \tag{5c}$$

To determine $\bar{P}$, 70 images of the Mie scattering of oil droplets (similar to that shown in Fig. 1a) were obtained for each flow condition. Images were normalized to account for laser intensity variations and were binarized; pixels having intensities exceeding half the maximum were set to a value of unity and all other pixel values were set to zero. The cross-sectional area of the reactants in the laser sheet, which is the area of the white region in Fig. 1a, was measured. The shape of the curve A–B–C was determined by superimposing the images and then fitting a parabola to this time-averaged flame position. It was required that the cross-sectional area under the resulting curve A–B–C equal the average cross-sectional area of the reactants in the 70 images. This area-matching requirement correctly accounts for large displacements of the flame to the right or to the left of centerline, and for large distortions of the flame shape as islands are formed. Isolated pockets of reactants are seen at the top of Fig. 1a; these pockets were included when determining the white area in Fig. 1a.

Use of the global turbulent burning velocity ($\bar{S}_T$) offers several advantages when the desire is to as-

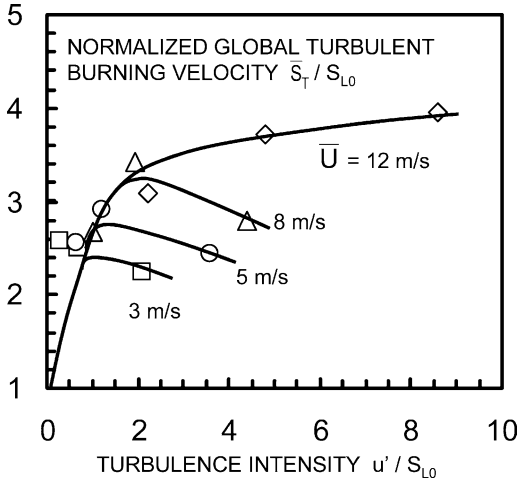

Fig. 2. Measured turbulent burning velocity, defined as global consumption speed $\bar{S}_T$. Conditions are listed in Table 1. For each curve, mean velocity $\bar{U}$ was held constant. Stoichiometric methane–air.

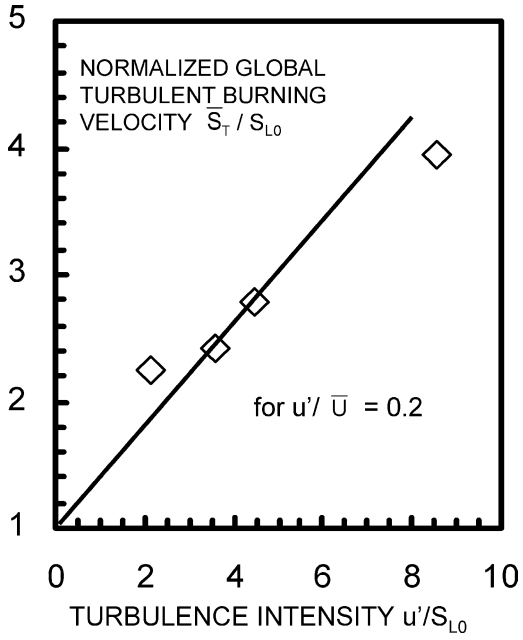

Fig. 3. Measured turbulent burning velocity replotted for a constant value of $u'/\bar{U} = 0.2$, so that u' and $\bar{U}$ are not independently varied. This method has been used previously and it incorrectly hides the true nonlinear behavior seen in Fig. 2.

sess the ability of a numerical simulation to predict the correct total consumption rate of reactants. Ambiguities and errors are eliminated because it is not necessary to measure the local velocity components, the location of the leading edge, or the normal to the flame brush, which are required for local displacement speed measurements [24]. Shepherd and Cheng [25] and Ghenai et al. [26] argued that for oblique flames, the consumption speed is a better measure of turbulent burning velocity than is the local displacement speed. Displacement speed has been shown to be three times larger than consumption speed [26] and is not a good measure of the local ability of the flame to convert reactants to products when the flame is oblique to the oncoming flow.

5. Results

5.1. Global consumption speeds $\bar{S}_T$

Fig. 2 is a plot of the measured values of turbulent burning velocity, which is defined as the global consumption speed $\bar{S}_T$ given by Eq. (5b). Mean velocity and turbulence levels u'/S_{L0} were varied up to the relatively large values of 12 m/s and 8.55, respectively. Two conclusions that can be drawn from Fig. 2 are that the mean velocity $\bar{U}$ is an important parameter for this category of flames, and that if $\bar{U}$ is held constant while u' is varied independently, the burning velocity curves display a nonlinear "bending." $\bar{U}$ is important because it affects the time that it takes eddies to cross the thin wrinkled reaction layer. This eddy residence time is defined as

$$t_{res} = \ell/(\bar{U}\sin\beta), \tag{6}$$

where ℓ is the integral scale and β is the angle between the x axis and the $\bar{c} = 0.5$ contour, so $\bar{U}\sin\beta$ is the component of the upstream velocity that is normal to the $\bar{c} = 0.5$ contour. In the present study, $\bar{U}$ was held constant while u' was increased by using a different grid, to increase the rotational velocity of the eddies while keeping the residence time approximately constant. This promotes the highly wrinkled, corrugated flame conditions that lead to flamelet merging and the "bending" phenomenon that has been reported in Refs. [27–32].

It is reasonable to expect that "bending" will occur, because as the turbulence level is increased, the flame surface area cannot grow indefinitely. Flamelets eventually merge and may extinguish due to strain. Gas expansion also creates divergent velocity fields that prevent segments from becoming too densely packed. When Duclos et al. [5] increased u'/S_{L0} above 5, the computed curves of burning velocity began to bend. Similarly, the bending of the measured curves in Fig. 2 begins when u'/S_{L0} is 2–4. Different explanations for the bending phenomenon have been offered by Peters [33], Bradley [28], and others [34–36].

It is noted that this "bending" would not occur if precautions were not taken to correctly vary u' and $\bar{U}$ independently. This is shown in Fig. 3. Data in Fig. 2 were replotted for a fixed value of $u'/\bar{U}$ equal to 0.2. The linear curve that appears in Fig. 3 represents results that would have been obtained if a single grid were employed and only the mass flow rate was varied, which usually has been done in the past. In such studies both the turbulence level and the residence time of eddies in the flame brush incorrectly were varied simultaneously. Thus, as u' and $\bar{U}$ increase, the eddies become stronger, but their residence time is reduced, and these two competing processes can counteract each other. This can mask the "bending" process and explain why it has not always been observed. The observation that $\bar{S}_T$ depends on $\bar{U}$ also helps to explain the large scatter observed when attempts were made to collapse values of $\bar{S}_T$ to a single curve. In those studies the values of $\bar{U}$ were allowed to vary randomly.

The global burning velocity measurements in Fig. 2 can be fit to the empirical relation

$$\frac{\bar{S}_T}{S_{L0}} = 1 + B_1\left[\left(\frac{u'}{S_{L0}}\right) - B_2\left(\frac{u'}{S_{L0}}\right)^2\right]^{1/2} \times \left[\frac{\bar{U}}{S_{L0}}\right]\left[\frac{\ell}{\delta_{L0}}\right]^{1/2}\left[\frac{W}{\delta_{L0}}\right]^{1/2}. \quad (7)$$

The values of constants B_1 and B_2 that provide the best fit of Eq. (7) to the data in Fig. 2 are 2.0×10^{-3} and 0.16, respectively, and δ_{L0} is 0.35 mm. The integral scale is ℓ and the thermal diffusivity α of a stoichiometric methane–air mixture is 0.20 cm^2/s. A physical explanation that leads to Eq. (7) is given by the scaling analysis below. The uncertainties in the data in Fig. 2 are approximately 6% and are discussed in Appendix A.

A question that arises is whether the nonlinear trend shown in Fig. 2 is due to changes in the surface area of the flame or to the internal structure of the flamelets as the turbulence intensity increases. To investigate this issue, the perimeter of the wrinkled flame surface was measured in 70 Mie scattering images and the averaged value of the wrinkled perimeter is P_T. Fig. 4 is a plot of $(P_T/\bar{P})^2$, where $\bar{P}$ is the perimeter of the smooth curve that represents the time-averaged flame position. This nondimensional parameter is one measure of flame wrinkledness and it displays the same trends as seen in Fig. 2; the curves bend as u' is varied, and the perimeter increases with $\bar{U}$. This indicates that changes in the surface area of the flame do play a major role in determining the trends in the burning velocity results.

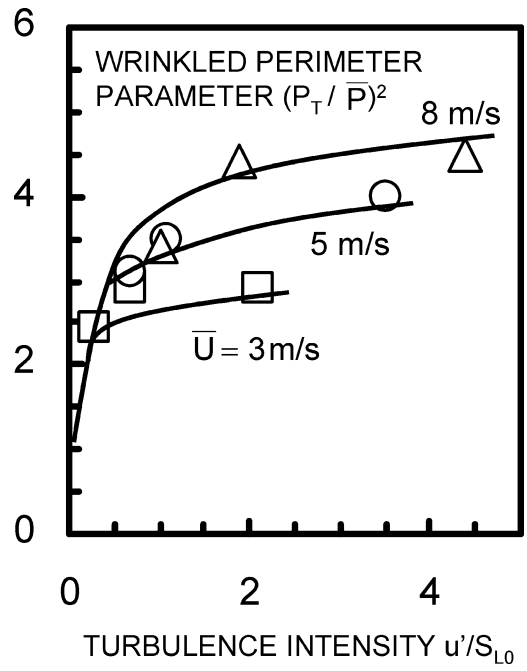

Fig. 4. Degree of flame wrinkling, quantified by the parameter $(P_T/\bar{P})^2$. P_T is the perimeter of the wrinkled flame surface that appears in the laser sheet images, averaged over 70 images. $\bar{P}$ is the perimeter of the smooth curve A–B–C in Fig. 1 that defines the time-averaged flame position. The trend displayed is similar to that of the turbulent burning velocity in Fig. 2.

5.2. Images of CH reaction layers, quenching rates, flame–eddy interactions

Figs. 5–7 show some images of the CH reaction layer and the vorticity field for relatively large values of the turbulence level ($u'/S_{L0} = 4.47$, case 8c) when "bending" is observed in Fig. 2. It is noted that pockets of reactants are seen in all of these figures, and the CH layers remain relatively thin, which indicates that the conditions are within the "corrugated flamelet regime." Fig. 5a is a magnified view of a region in Fig. 5b. An "eddy" is defined as a region where the magnitude of the instantaneous vorticity exceeds 2000 s^{-1}; this value was chosen to identify the main features of the flow; less intense vortical regions also exist but they are not shown. The red eddies are associated with counterclockwise rotational velocities. To visualize the gas velocity near each eddy, the measured instantaneous velocity vectors are plotted in Figs. 5–7. The mean velocity of the reactants at the center of each image has been subtracted from the velocity at every location, which explains why some of the vectors point downward. Note that the vectors represent the instantaneous gas velocity in the laboratory frame of reference, and not the flame frame

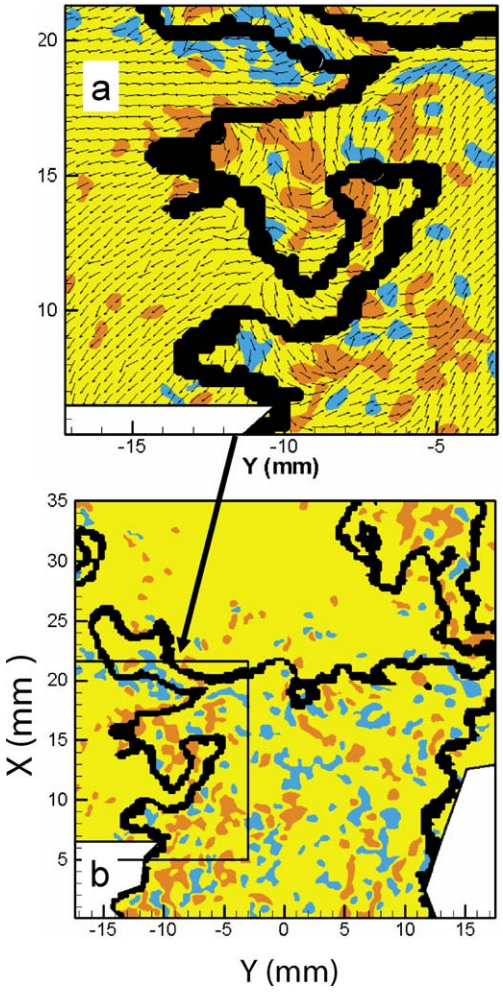

Fig. 5. Images of the CH reaction layers (black) and the turbulent eddies (red and blue) for case 8c. $\bar{U} = 8$ m/s. $u'/S_{L0} = 4.47$. Red and blue regions have vorticity magnitude exceeding 2000 s^{-1}. Stoichiometric methane–air. (a) Magnified view of a 15 × 22-mm region, reactants are on the right, products are on the left; (b) entire field of view (35 × 35 mm); reactants are in the middle region. In the white regions the particle seeding density was insufficient.

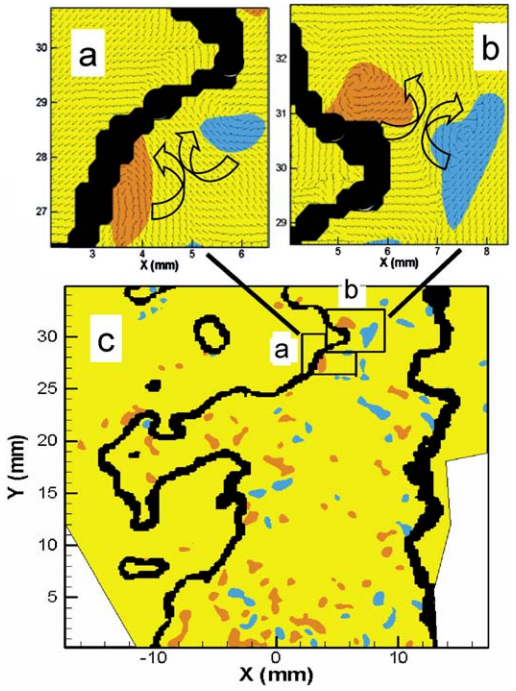

Fig. 6. Another image of the CH reaction layers (black) and the turbulent eddies (red and blue) for case 8c. $\bar{U} = 8$ m/s. $u'/S_{L0} = 4.47$. Red and blue regions have vorticity magnitude exceeding 2000 s^{-1}. Stoichiometric methane–air. (a, b) Magnified regions 4.5 × 4.5 mm; (c) full field of view 35 × 35 mm.

of reference, so they do not always point toward the flame on the reactant side and away from the flame on the product side, since the flame is not stationary. The CH layers are shown as wrinkled black lines; they are the locations where the CH PLIF signal exceeds half the local maximum signal.

The images indicate that there is intense wrinkling of the CH layers and that the eddies are numerous on the reactant side, but are less numerous on the product side. This observation is consistent with the flame–vortex studies of Mueller et al. [38], who reported that most of the vorticity is destroyed as an eddy crosses a premixed flame, because gas expansion spreads the rotational angular momentum over a large region in space. Figs. 5–7 also illustrate the relative roles of flamelet merging and quenching, which can cause the "bending" behavior described above. It is seen that the CH layers are continuous, unlike the discontinuous CH layers reported in the nonpremixed swirl flame of Ratner et al. [23]. Quenching is defined to occur where the CH signal on the layer centerline is less than 25% of the maximum CH signal in the image. No regions of flamelet quenching were observed in any of the 1500 CH PLIF images. Therefore it is concluded that in the present work, local flame quenching is not a possible reason for the "bending" phenomenon, and that

$$\bar{Q} = 0. \tag{8}$$

Figs. 5–7 offer evidence that merging of flamelets does occur, but the rate of merging cannot be quantified with the present diagnostics. Merging is about to occur wherever there are two CH reaction layers that are propagating toward each other, with only a thin layer of reactants between them. This is seen in Fig. 5b, where there is a "neck" region at the top of the boxed region and another neck region on the far right side. A neck region is beginning to form in

Fig. 6 at $y = 20$ mm. Evidence that merging has just occurred is the existence of the pockets of reactants that are seen in Fig. 6c. Pockets can be caused only by flamelet merging. First, long fingers of the wrinkled flame surface are created, as seen in Figs. 5–7, which look like those observed in the flame–vortex interactions of Refs. [37–40]. Then as the CH layers propagate toward each other, they often form a neck that burns through to create a pocket. The merging of flamelets and the creation of pockets can reduce the reaction zone surface area. When the turbulence intensity u'/S_{L0} is reduced from 4.47 to less than one (cases 3a, 3b, and 5a), very few peninsulas or pockets are observed. This is evidence that the merging rate increases with turbulence level. The images of the neck regions in Fig. 5 are similar to DNS of flamelet merging reported by Chen et al. [37, Fig. 12] for an u'/S_{L0} value of 10.

The images indicate that the wrinkles in the CH reaction layers are significantly larger than even the largest eddies. The eddies in Figs. 5–7 vary from a maximum size of 3 mm to a minimum of 0.3 mm (the detecting limit for the PIV measurement); the average size is about 1–2 mm. The average radius of curvature of the CH layer was measured to be 12.5 mm, which is more than six times the average eddy size. This difference is consistent with previous studies of flame–vortex interactions [37–40]. As an eddy approaches the flame, the gas expansion creates a dilatation velocity that greatly exceeds u', so an eddy cannot roll up the flame and create a radius of curvature comparable to its own radius.

Figs. 6a and 6b show counterrotating eddy pairs which exert extensional and compressive strain on the flame. These are magnified views of the regions denoted A and B in Fig. 6c. To better visualize the rotating velocity pattern, a constant-velocity vector was subtracted from each PIV image. Note that in Fig. 6b the flame is curved in the direction of the velocity vectors; it appears that the flame is pulled into the region between the two eddies, imparting a large curvature to the CH layer. In theory, a purely compressive strain field should reduce the flame area, as negative strain exerts a negative stretch rate; however, the eddies in Fig. 6b are affecting both the strain rate and the curvature, and it is likely that the flame area would increase if the CH layer were advected in the direction of the velocity vectors. In Fig. 6a the eddy pairs exert extensional (positive) strain, similar to that observed in a counterflow geometry. Note that the CH layer is thinner between the two eddies, which is expected in a positive strain field. These flame–eddy interactions in a fully turbulent flame are similar to the single flame–vortex experiments of Mueller et al. [38] and Sinibaldi et al. [39] and the simulations of Najm and Wyckoff [40]. In Fig. 7a a large eddy exists

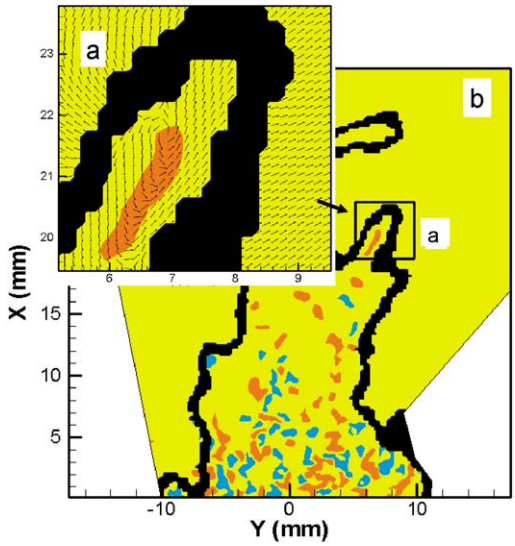

Fig. 7. Images of the CH reaction layers (black) and the turbulent eddies (red and blue) for case 3c. $\bar{U} = 3$ m/s. $u'/S_{L0} = 2.14$. Red and blue regions have vorticity magnitude exceeding 2000 s^{-1}. Stoichiometric methane–air. (a) Magnified view of a 4.5 × 4.5-mm region; (b) full field of view of a 35 × 35-mm region.

within an elongated flame wrinkle. However, in most of the elongated flame wrinkles, no such large eddy is seen. The fact that the large wrinkles do not correlate with the presence of large eddies nearby may be due to the possibility that a large eddy previously created the wrinkle but now has disappeared. Another possibility is that the eddies trigger hydrodynamic or thermodiffusive instabilities in the flame, which have their own characteristic wavelengths.

5.3. Stretch rates, stretch efficiency factor Γ_K, quenching rates

The stretch rate (K) along the CH layers is the sum of the strain rate K_s and the curvature contribution K_c [11]:

$$K = K_s + K_c, \tag{9}$$

$$K_s = -\mathbf{n}\cdot(\mathbf{n}\cdot\nabla)\mathbf{V}_G + \nabla\cdot\mathbf{V}_G, \tag{10a}$$

$$K_c = S_L/R_c. \tag{10b}$$

To measure the in-plane component of K, the isoline of the maximum CH signal was identified along with its normal. This isoline is located along the center of the thin black CH layers seen in Figs. 5–7. Then the leading edge of the flame was defined as a second isoline that is 0.4 mm closer to the reactants than the first isoline, and the in-plane components of gas velocity ($\mathbf{V}_G$) were measured on this second isoline using algorithms described in Ref. [22] and Appendix A. Experimental uncertainties are introduced because

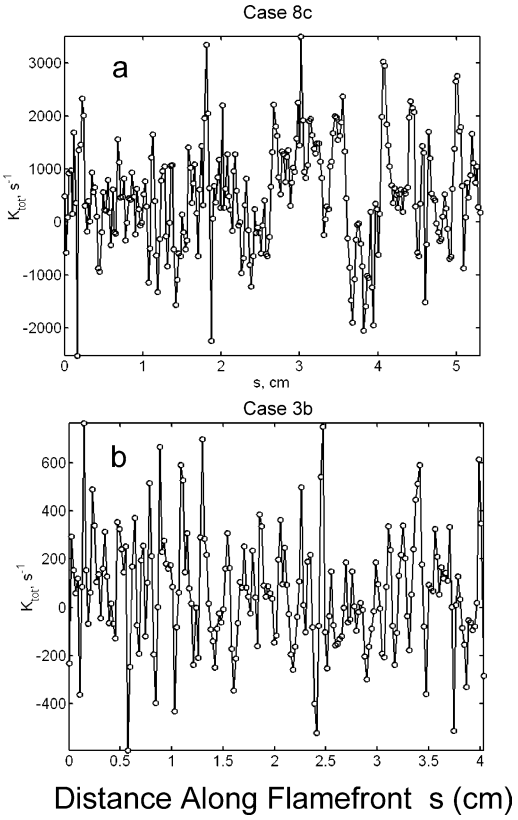

Fig. 8. (a) Instantaneous stretch rate (K) measured in the tangential direction (s) along the wrinkled CH reaction layer for case 8c using simultaneous PIV/CH PLIF diagnostics. Mean stretch rate is 366 s^{-1}. (b) Instantaneous stretch rate for case 3b; mean stretch rate is 84 s^{-1}.

(1) only the in-plane components of velocity and radius of curvature (R_C) could be measured,
(2) contributions from scales less than the PIV spatial resolution (0.3 mm) were not resolved, and
(3) the local propagation speed has been replaced by the unstretched laminar value in Eq. (10b).

Estimates of these uncertainties are reported in Appendix A.

Fig. 8a illustrates the instantaneous stretch rates K along the leading edge isoline for case 8c at $x = 26$ mm. It is seen that stretch rates oscillate between approximately $+2000$ and -1000 s^{-1}; the mean stretch rate for this case (8c) is listed in Table 2; it is 366 s^{-1}. Fig. 8b is a plot of stretch rates for case 3b at $x = 56$ mm. K oscillates between ± 400 s^{-1} and its mean value is 84 s^{-1}, which appears in Table 2. For all cases listed in Table 2, the mean stretch rate is positive, as expected. Note that the adjacent data points in Fig. 8 are reasonably well correlated; there are typically four to six data points that are either monotonically increasing or decreasing on each small segment of the curve. If random errors were excessive, the adjacent data points would not display this degree of correlation.

The large maximum instantaneous values of stretch rate in Fig. 8a, which exceed 1000 s^{-1}, may be due to several factors. The turbulent velocity fluctuation (u') for case 8c was about 2 m/s, and eddies with a diameter of 2 mm are observed in Fig. 5. The ratio of these numbers is 1000 s^{-1}. Also, large stretch rates were found to occur where the CH layer undergoes a 90° bend. At these locations the tangential velocity typically was 8 m/s where the flamelet is parallel to the mean flow, but was nearly zero at a location 8 mm away where the flamelet was perpendicular to the mean flow. This change of 8 m/s in an 8-mm region leads to a stretch rate of 1000 s^{-1}.

A stretch rate of 1800 s^{-1} is required [41] to extinguish a steady, counterflow, stoichiometric methane–air flame at 1 atm with a reactant temperature of 296 K. There are some locations in Fig. 8a where the instantaneous stretch rate exceeds this value, but the CH reaction layer does not extinguish anywhere. Extinction requires that a sufficient stretch rate be imposed for a sufficient residence time, but eddies pass through the present flame with large convection velocities that are 10 times larger than those used in flame–vortex computations and experiments [12,37–40], so the residence time defined by Eq. (6) is small. Donbar et al. [22] found that nonpremixed turbulent flames also do not extinguish where the strain rate exceeds the steady-state extinction limit because of unsteady effects.

The stretch efficiency factor Γ_K was determined by dividing the measured mean stretch rates in Table 2 by the values of u'/ℓ listed in Table 1. Fig. 9 shows that Γ_K increases as the square of the integral scale, which is consistent with the flame–vortex DNS of Meneveau and Poinsot, as was shown in Fig. 14 of Ref. [12]. Thus, larger eddies in our turbulent flame are more efficient at stretching the flame than the small eddies; this finding is similar to that of the flame–vortex computations [12]. Fig. 9 also indicates that as the mean velocity of the Bunsen burner is increased, there also is an increase in the stretch efficiency factor. This can be explained by the fact that larger mean velocities force the flame to become taller, and the farther a flame segment is located away from the rim (which anchors the base and prevents wrinkling), the more wrinkled the segment becomes. A wrinkled flame has a larger probability that the segment will undergo a sharp bend, which causes the velocity that is tangential to the flame to change abruptly, leading to a large stretch rate. In addition, for a taller flame, the residence time of eddies in the brush is larger than the situation for which eddies travel normal to the flame brush. A reasonable curve fit to the

Table 2
Measured values of the mean stretch rate ($\bar{K}$), mean strain rate ($\bar{K}_s$), mean curvature contribution ($\bar{K}_c$), the standard deviations, and the stretch efficiency function Γ_K

Case	x (mm)	$\bar{K}$ (s^{-1})	$\bar{K}_s$ (s^{-1})	$\bar{K}_c$ (s^{-1})	σ (s^{-1})	σ_s (s^{-1})	σ_c (s^{-1})	Stretch efficiency function Γ_K
3b	21	79	76	2.7	271	229	146	1.57
3b	56	86	94	−8.4	349	278	211	1.71
3c	13	184	165	19	670	581	333	0.70
3c	31	174	141	33	448	361	265	0.66
8b	26	223	226	−3.0	1155	1106	333	4.00
8b	61	248	239	9.1	910	849	329	4.44
8b	96	229	241	−12	861	816	275	4.10
8c	26	389	386	3.0	972	909	345	1.99
8c	61	232	238	−5.7	1155	1107	331	1.19

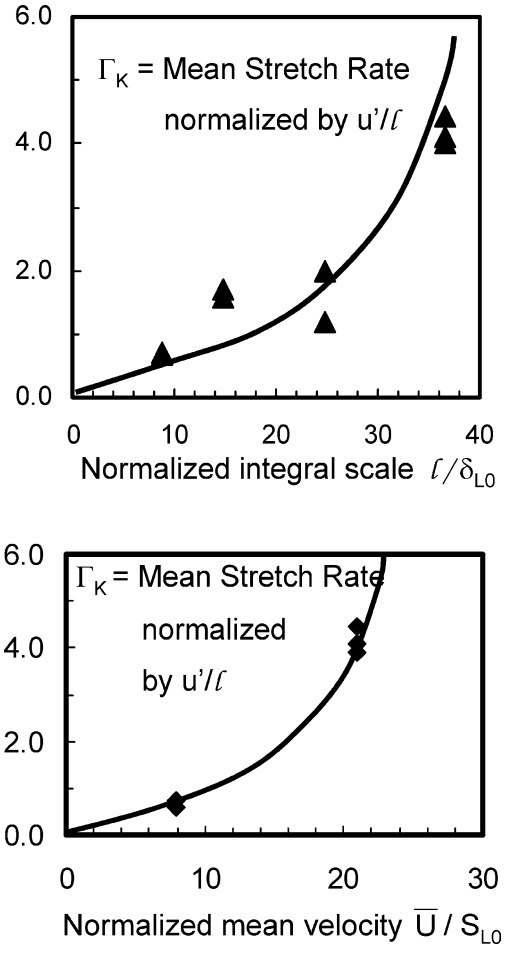

Fig. 9. Measured stretch efficiency factor (Γ_K) showing that large eddies and a large mean velocity lead to more efficient stretching of the flame surface. Values of stretch rate are listed in Table 2. Laminar flame thickness δ_{L0} is 0.35 mm.

data in Fig. 9 is

$$\Gamma_K = C_1 \left(\frac{\ell}{\delta_{L0}}\right)^2 \left(\frac{\bar{U}}{S_{L0}}\right)^2. \tag{11}$$

The constant C_1 is determined to be 6.6×10^{-6}, based on a laminar flame thickness δ_{L0} ($= 7.4\alpha_{L0}/S_{L0}$) equal to 0.35 mm. Fig. 10 shows that the probability density functions (pdf) of the measured strain rates K_s and flame curvature are nearly Gaussian functions. Values of the means and standard deviations of the pdf values are listed in Table 2.

5.4. A scaling relation that explains the burning velocity trends

A scaling analysis was conducted to better understand the physical reasons why burning velocities in Fig. 2 depend on mean velocity $\bar{U}$ and burner width W, and why the curves display "bending." It is now shown that Eq. (7), which is an empirical curve fit to the data, can be derived from the conservation equation for flame surface density. Consider a turbulent Bunsen flame that is fairly tall so that the contour of mean reactedness $\tilde{c} = 0.5$ is nearly aligned with the mean flow velocity $\bar{U}$. This will be denoted the tall flame assumption. The x direction is nearly parallel to the flame brush and the coordinate normal to the brush (η) can be approximated by y. The Σ equation (Eq. (2)) is multiplied by dy and integrated from $y = 0$ to $+\infty$:

$$\int_0^\infty \bar{U}\frac{\partial \Sigma}{\partial x}\,dy + \int_0^\infty \bar{V}\frac{\partial \Sigma}{\partial y}\,dy = \int_0^\infty \nu_T \frac{\partial^2 \Sigma}{\partial y^2}\,dy + \int_0^\infty (\bar{K} - \bar{m})\Sigma\,dy. \tag{12}$$

In Eq. (12) the quenching term $\bar{Q}$ has been neglected because no quenching is observed, as stated by Eq. (8). A new merging quantity $\bar{m}$ has been defined to be $\bar{M}/\Sigma$. Because flame brush is assumed to be nearly vertical, the second term in Eq. (12) can be neglected, as $\bar{V}$ is much less than $\bar{U}$. The third term in Eq. (12) is zero, because, after integration, it

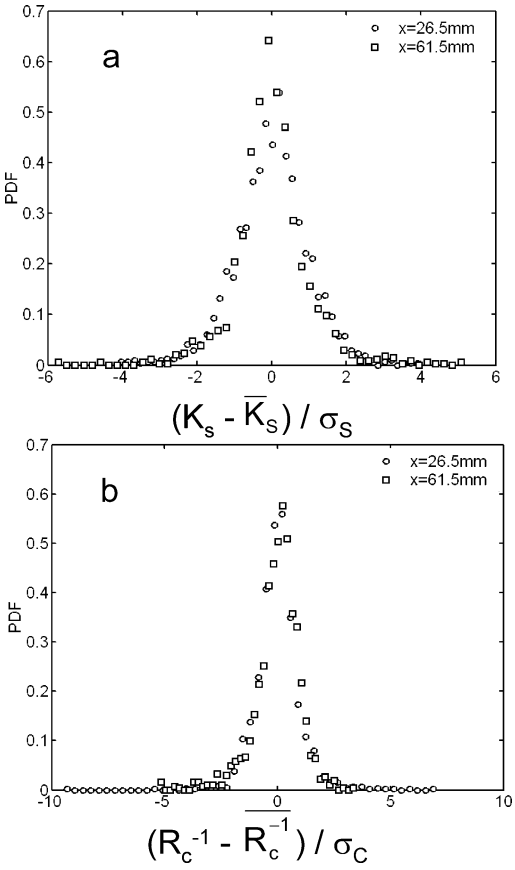

Fig. 10. Probability density functions of (a) the strain rates and (b) flame curvature for case 8c. $\bar{U} = 8$ m/s. $u'/S_{L0} = 4.47$. Mean values and standard deviations are given in Table 2.

is the difference between $\partial\Sigma/\partial y$ evaluated at $y = 0$ and infinity; both of these values are zero. For simplicity, it is assumed that the following quantities do not vary in space: $\bar{K}$, $\bar{m}$, the turbulent diffusivity ν_T, $\bar{U}$, u', and the integral scale. These assumptions are not realistic but the goal is to integrate the equations under ideal conditions to show why certain governing parameters appear. The quantity $\int \Sigma\, dy$ equals approximately $(S_T/S_{L0})\, I_0^{-1}$ because of Eq. (1), and I_0 is approximately equal to unity for stoichiometric methane–air reactants. Therefore Eq. (12) can be rearranged to yield

$$\bar{U}\, d(S_T/S_{L0})/dx = (\bar{K} - \bar{m})(S_T/S_{L0}), \tag{13a}$$

which is

$$(S_T/S_{L0})^{-1}\, d(S_T/S_{L0}) = \left[(\bar{K} - \bar{m})/\bar{U}\right] dx. \tag{13b}$$

Integration yields

$$S_T/S_{L0} = \exp\left[(\bar{K} - \bar{m})x/\bar{U}\right]. \tag{13c}$$

The right-hand side of Eq. (13c) is expanded in a series and becomes $(1 + [(\bar{K} - \bar{m})x/\bar{U}])$ plus higher-order terms which are neglected. To justify neglecting the higher-order terms, note that values in Tables 1 and 2 indicate that $\bar{K} = 223\ \mathrm{s}^{-1}$ when $\bar{U} = 8$ m/s, $x = 26$ mm; the second-order term in the expansion can be shown to be less than 25% of the first-order term. The global burning velocity $(\bar{S}_T)$ is defined as the average value of the local burning velocity (S_T), so that

$$\bar{S}_T/S_{L0} = H^{-1} \int_0^H (S_T/S_{L0})\, dx, \tag{14}$$

where H is the average height of the Bunsen flame. Combining Eqs. (13c) and (14) yields

$$\bar{S}_T/S_{L0} - 1 = (1/2)(\bar{K} - \bar{m})(H/\bar{U}). \tag{15}$$

The physical meaning of Eq. (15) is clear; the global propagation speed depends on the product of the effective stretch rate $(\bar{K} - \bar{m})$ and the geometric time scale $(H/\bar{U})$, which represents the time for an eddy to travel along the flame from the base to the tip. That is, wrinkling is due to a sufficiently large rate of stretching of the surface that is applied for a sufficiently long time. The height of any Bunsen flame (H) can be approximated by the geometric relation $(W/2)(\tan\beta)^{-1}$, where β is half of the included angle at the tip. From geometry, $\bar{S}_T$ is $\bar{U}\sin\beta$, and for small angles $\sin\beta = \tan\beta$, so

$$H = (W/2)(\bar{U}/\bar{S}_T). \tag{16}$$

Now Eq. (16) is inserted into Eq. (15) to yield

$$\bar{S}_T/S_{L0} = 1 + 0.5(W/S_{L0})^{1/2}(\bar{K} - \bar{m})^{1/2}. \tag{17}$$

Conditions are assumed to be consistent with the tall flame approximation discussed above, so the ratio $\bar{S}_T/S_{L0}$ is much greater than unity. The stretch efficiency function (Γ_K) and the merging efficiency function (Γ_M) are defined in the same manner as is done in Ref. [12]:

$$\bar{K} = (u'/\ell)\Gamma_K, \tag{18a}$$

$$\bar{m} = (u'/\ell)\Gamma_M. \tag{18b}$$

Combining Eqs. (17) and (18) yields

$$\bar{S}_T/S_{L0} = 1 + 0.5(W/\ell)^{1/2}(u'/S_{L0})^{1/2} \times (\Gamma_K - \Gamma_M)^{1/2}. \tag{19}$$

As stated in the previous section, the measured values of Γ_K in Fig. 10a and 10b are best fit by

$$\Gamma_K = C_1(\ell/\delta_{L0})^2(\bar{U}/S_{L0})^2. \tag{20a}$$

The merging rate $\bar{m}$ was not measured so the quantity Γ_M in Eq. (18b) can only be estimated using the relation

$$\Gamma_M = C_2(u'/S_{L0})(\ell/\delta_{L0})^2(\bar{U}/S_{L0})^2. \quad (20b)$$

This estimate is based on the observation that flamelet merging increases when the stretch rate increases (as the flame becomes more wrinkled), so it is logical that Γ_M is proportional to Γ_K. It also is noted that Eq. (20b) can be justified entirely on empirical grounds. This analysis is not a prediction that is based on first principles; instead, Eq. (20b) seems to provide a good empirical fit to the measured burning velocities. If the laminar flame thickness δ_{L0} in Eqs. (20a) and (20b) is replaced by its known value of α_0/S_{L0} and Eq. (19) is combined with (20a) and (20b), it follows that

$$\frac{\bar{S}_T}{S_{L0}} = 1 + B_1\left[\left(\frac{u'}{S_{L0}}\right) - B_2\left(\frac{u'}{S_{L0}}\right)^2\right]^{1/2} \times \left[\frac{\bar{U}}{S_{L0}}\right]\left[\frac{l}{\delta_{L0}}\right]^{1/2}\left[\frac{W}{\delta_{L0}}\right]^{1/2}. \quad (21)$$

This relation is the same as Eq. (7), which represents a reasonable fit to the measurements in Fig. 2. The values of constants B_1 and B_2 are 2.0×10^{-3} and 0.16, respectively.

Eq. (21) is useful in that it identifies the burner width W as a category-dependent parameter. For the Bunsen burner (envelope flame) category, a wider burner leads to a taller flame, which becomes more wrinkled than a short flame, and this increases $\bar{S}_T$. Eq. (21) also explains why the burning velocity curves in Fig. 2 depend on mean velocity. Increasing $\bar{U}$ does several things: it reduces the residence time (Eq. (6)) if the flame height is held constant, but it also has the competing effect of making the flame longer, which tends to increase the residence time. Increasing $\bar{U}$ changes the orientation between the flame brush and the streamlines, which also affects the eddy residence time.

The above analysis indicates that the "bending" is due to two factors: the merging of flamelets and a geometric factor associated with Bunsen flames. Merging of flamelets tends to cause a decrease in the flame surface area and $\bar{S}_T$ as u' increases. The geometric factor that causes bending is associated with flame height; increasing the turbulence level tends to make the flame propagate faster, but this is counteracted by the fact that a faster Bunsen flame becomes shorter (Eq. (16)), which reduces the residence time ($H/\bar{U}$ in Eq. (15)) during which stretch is applied.

Eq. (21) contains the factor $\bar{U}$ on the right-hand side, and this result is consistent with the measured curves in Fig. 2, which display increasing height as $\bar{U}$ increases. Eq. (21) also indicates that $\bar{S}_T$ should increase as the laminar burning velocity S_{L0} increases. Therefore $\bar{S}_T$ should be maximum if the fuel–air ratio is nearly stoichiometric, which is realistic. Some previous formulas for S_T are unrealistic because they indicate that S_T becomes independent of S_{L0} at sufficiently large turbulence levels; this implies that the propagation speed does not approach zero as the equivalence ratio approaches zero, which is unrealistic.

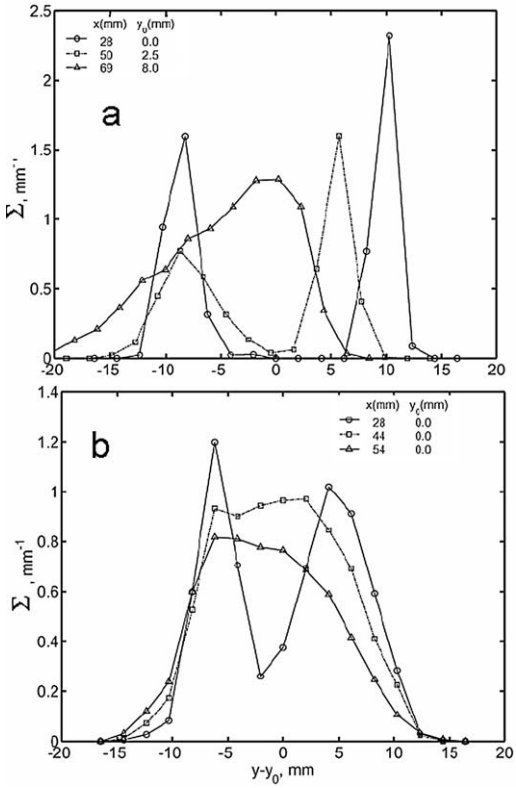

Fig. 11. Flame surface density (Σ) measured for (a) case 3b and (b) case 3c. $\bar{U} = 3$ m/s. $u'/S_{L0} = 0.69$ and 2.14, respectively.

5.5. *Flame surface density, wrinkling, thickness of flamelets*

Profiles of flame surface density (Σ) appear in Figs. 11 and 12 for four operating conditions. To determine Σ, it was assumed that the average flame surface area per unit volume equals the average flame perimeter per unit area in the laser sheet. At each location of interest, an interrogation box of size 2.05×2.05 mm was chosen. Each image of the CH signal was binarized; the values associated with pixels within the CH layer (where the CH intensity is more than half of its maximum value) were set to unity (black); all other pixels were assigned a value of zero

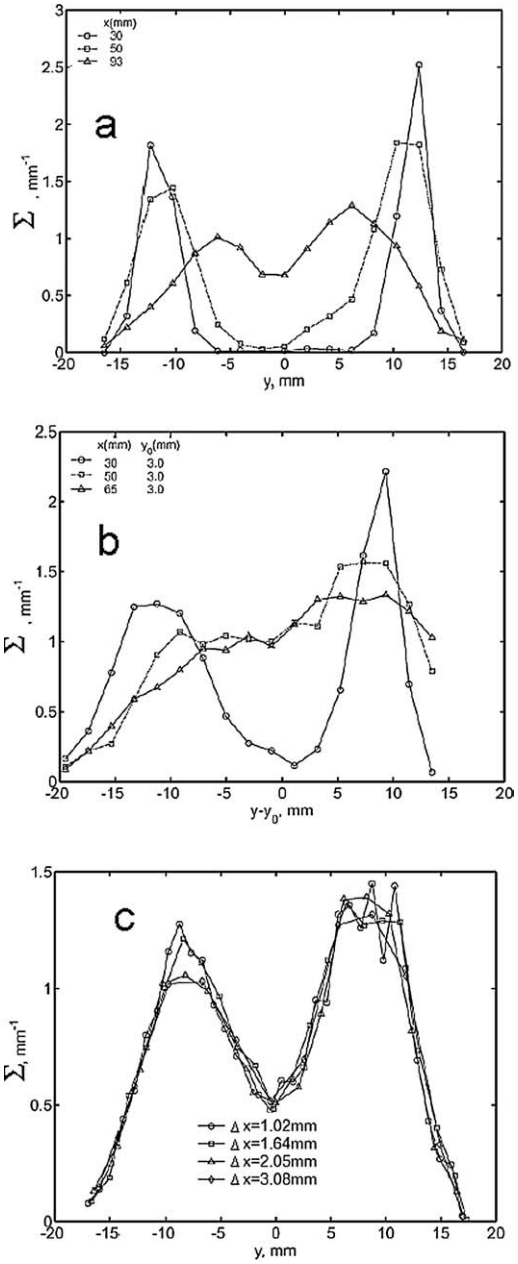

Fig. 12. Flame surface density (Σ) measured for (a) case 8b and (b, c) case 8c. $\bar{U} = 8$ m/s, $u'/S_{L0} = 1.88$ and 4.47, respectively. Lowest figure indicates that as the interrogation box size was reduced from 3.08 to 1.02 mm, no significant change in Σ resulted.

(white). The average perimeter of CH layers in the box is the average area of the black pixels within the box, divided by the average thickness of the CH layer at that location. Fig. 12c shows that varying the box size from 1.02 to 3.08 mm does not affect values of Σ determined in this way. A larger box has

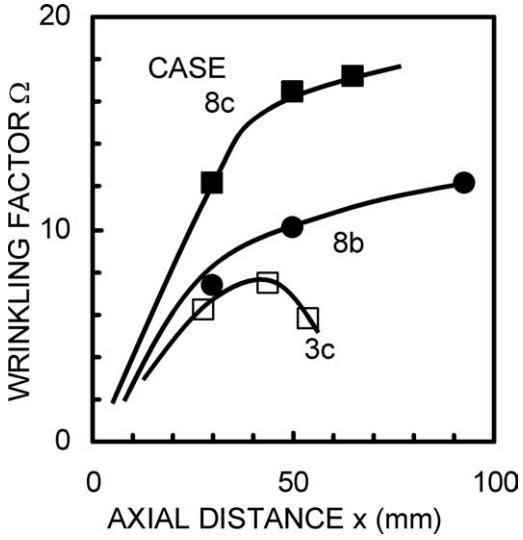

Fig. 13. Measured nondimensional wrinkling parameter Ω, defined as $(1/2)\int_{-\infty}^{+\infty} \Sigma\, dy$. Values of Σ used to determine Ω are plotted in Fig. 12. Flames become more wrinkled in the x direction, but some bending of each curve occurs.

a higher probability of containing a CH layer, leading to a larger mean perimeter, but when this larger perimeter is divided by the larger box area no change in Σ results. As expected, the profiles of Σ have the shape of two delta functions near the burner exit, and become Gaussian-shaped near the flame tip. The profiles in Figs. 11 and 12 do display some asymmetry, which is due to flow nonuniformities in the burner internal flow field.

It is useful to define a wrinkling parameter Ω to quantitatively determine if future DNS results predict the same degree of flame wrinkling as is found in experiments. It has been shown [10,15] that the integral of Σ across the flame brush is a good measure of the degree of wrinkling of the reaction zone, so we define a wrinkling parameter (Ω):

$$\Omega = \frac{1}{2}\int_{-\infty}^{+\infty} \Sigma\, dy. \tag{22}$$

The factor $1/2$ occurs because we are integrating over two flame brushes—one on the right and one on the left side of the burner. Fig. 13 is a plot of values of Ω obtained by integrating the profiles of Σ in Figs. 11 and 12. As expected, the flames become more wrinkled in the x direction, and wrinkling increases as u' is increased. A larger mean velocity (case 8) yields more wrinkling because the flame is taller and the flame–vortex residence time (Eq. (6)) is increased. Some bending of the curves in Fig. 13 is observed.

Another parameter that must be modeled correctly is the thickness of the chemical reaction zones.

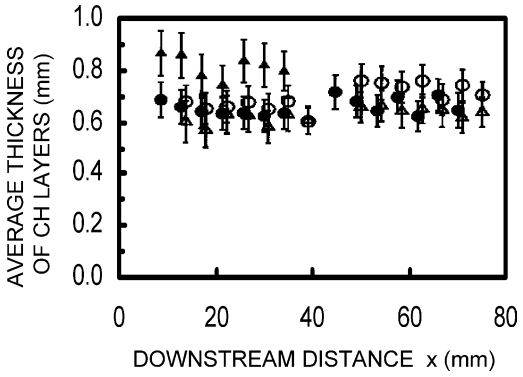

Fig. 14. Average thickness of the CH reaction layers ($\bar{\delta}_{CH}$) measured in four flames, in which the turbulence intensity u'/S_{L0} changes by a factor of 5, from 0.69 (case 3b) to 4.47 (case 8c). Note that CH reaction layer thickness is not significantly affected by turbulence intensity. ●, case 3b; ▲, case 3c; ○, case 8b, △, case 8c.

The CH reaction zones are the thin black regions in Figs. 5–7; they appear to have a fairly uniform thickness of 0.6 to 0.8 mm and are not broadened by more than a factor of 2 at any location except where merging is occurring. Fig. 14 is a plot of the average thickness of the CH layers ($\bar{\delta}_{CH}$), which is the full-width distance between points where the CH signal is half of its maximum intensity. For these four conditions the turbulence intensity varies by a factor of 5 (from $u'/S_{L0} = 0.69$ to 4.47) yet the layer thickness $\bar{\delta}_{CH}$ remains at a constant value of approximately 0.7 mm. Therefore, it is concluded that there is no significant change to the measured thickness of the CH layers even when there are large changes in the turbulence level and the spatial location. The uncertainty in the values of CH layer thickness is 0.2 mm, which is the thickness of the laser sheet and the spatial resolution of each binned 3×3-pixel region. The bars plotted in Fig. 14 represent the precision in the determination of the mean based on averaging 70 images.

Based on the results in Figs. 5–7 and 14, it is concluded that flamelets are observed to exist for our conditions (and not distributed reaction zones), although it cannot be determined if they are "laminar" flamelets or "thickened" flamelets. Peters [33] defines a flamelet as a reaction layer in which the gradients of scalars (such as CH concentration) that are normal to the layer are much larger than the tangential gradients. Analysis of the CH gradients indicates that the thin (0.7 mm thick) CH layers in images such as Figs. 5–7 meet this criterion. It cannot be determined if the flamelets are "laminar," which would require that the molecular diffusivity in the preheat zone greatly exceeds the turbulent diffusivity. It also cannot be determined if the flamelets are "thickened" by turbulence. Dinkelacker [42] provides images of flamelets for which turbulence eddies enter and modify the preheat zone.

If a distributed reaction zone existed, it is expected that the thickness of the CH reaction zone would increase with the turbulent diffusivity ($u'\ell$). However, the measured mean values in Fig. 14 suggest that such an increase does not occur, even when u' is increased by a factor of 5. It is noted that the actual layer thickness may be somewhat less than the values in Fig. 14, for two reasons. The instantaneous CH layer thickness is, in many locations, at the limit of the spatial resolution of 0.2 mm. This resolution limit most strongly biases the thinnest flamefront segments. Thus the true thickness of the layers is expected to be less than the 0.7 mm value shown in Fig. 14. Another reason the true thickness is expected to be less than 0.7 mm is that the flame surface is not normal to the laser sheet. Based on the data of Shepherd and Ashurst [43] the actual 3D layer thickness is the 2D value (i.e., the value plotted in Fig. 14) multiplied by the direction cosine that is denoted $\bar{\sigma}_\theta$ and has a typical value of 0.65 [43]. Thus we expect that the average 3D CH layer thickness is 0.5 mm, which is 65% as large as the values in Fig. 14. Shepherd and Ashurst also found that as the turbulence level varied, the ratio of 3D to 2D layer thickness did not vary significantly. It can be concluded that the mean thickness of the CH reaction zones in our flamelets is less than 0.7 mm. A detailed study of the structure of the flamelets would require a spatial resolution that is significantly less than our value of 0.2 mm.

Previous work also is in general agreement with the present findings; Shepherd et al. [44] increased u' by a factor of three and observed no change in the thicknesses of thermal layers that they measured using Rayleigh scattering. Tanahashi et al. [45] increased u' by a factor of two in their direct numerical simulations and report no increase in the computed reaction zone thickness. For a nonpremixed jet flame, Donbar et al. [22] showed that for jet Reynolds numbers up to 18,600, the CH layers remained thin and were no thicker than 1 mm.

The thickness of the flame brush (δ_T) is defined as the full width at half-maximum of the profiles of c'_{rms}, where c is the reactedness. Values of δ_T are plotted in Fig. 15. The brush thickness increases in the x direction, and it increases as the level of turbulence increases, as expected. Reactedness (c) was determined from the CH PLIF images by assigning a value of c equal to zero to the reactants and a c of one to the products. Across the thin CH reaction layer, the value of c varied in a linear manner. The profiles of $\bar{c}$ and c'_{rms} are adequately fit by an error function and a Gaussian function, respectively,

$$\bar{c} = 0.5\big(1 + \mathrm{erf}\big((y - y_0)/\delta_T\big)\big), \tag{23}$$

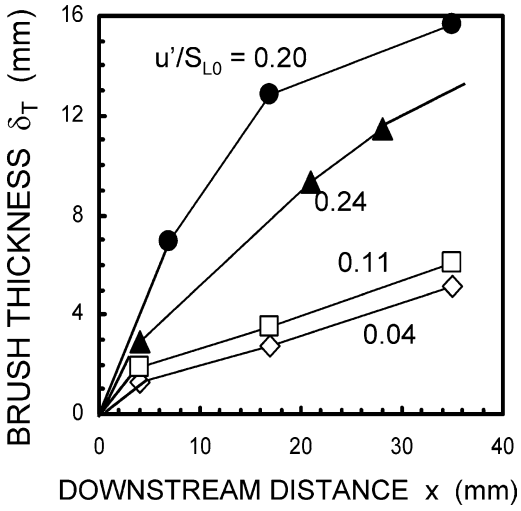

Fig. 15. Thickness of the turbulent brush (δ_T) measured for cases 3b, 3c, 8b, and 8c. δ_T is the FWHM of the profiles of the rms fluctuations of the reactedness. Conditions for each case are listed in Table 1.

$$c'_{\mathrm{rms}}/c'_{\mathrm{rms,max}} = \exp\left(-0.5\left((y-y_0)/\delta_T\right)^2\right), \qquad (24)$$

where y_0 is the lateral coordinate of the center of the flame brush. Therefore, using the values of δ_T plotted in Fig. 15, one can use Eqs. (23) and (24) to represent the profits of $\bar{c}$ and c'_{rms} in the present experiment.

6. Conclusions

(1) A comprehensive data set describes previously unreported properties of a turbulent premixed flame that are especially useful for the assessment of direct numerical simulations and models, including local stretch rates, a wrinkledness parameter, degree of flamelet extinction, reaction layer thicknesses, flame surface density (Σ), and global consumption speed, which is one type of turbulent burning velocity.

(2) The global turbulent burning velocity ($\bar{S}_T$) of a Bunsen flame displays nonlinear dependence ("bending") as the turbulence level (u'/S_{L0}) is increased above the relatively large values of 4–8, if the burner width (W) is made sufficiently large, and if u' and $\bar{U}$ are varied independently. The perimeter of the wrinkled flame (P_T) displays similar bending behavior.

(3) Global turbulent burning velocities were best fit to the empirical relation

$$\frac{\bar{S}_T}{S_{L0}} = 1 + B_1\left[\left(\frac{u'}{S_{L0}}\right) - B_2\left(\frac{u'}{S_{L0}}\right)^2\right]^{1/2} \times \left[\frac{\bar{U}}{S_{L0}}\right]\left[\frac{\ell}{\delta_{L0}}\right]^{1/2}\left[\frac{W}{\delta_{L0}}\right]^{1/2},$$

which indicates that two additional parameters are required to correlate Bunsen flame data: the mean velocity ($\bar{U}$) and burner width (W), both of which affect the residence times of flame–eddy interactions. A scaling analysis was developed to explain the observed dependence on $\bar{U}$ and W and the nonlinear dependence on u'.

(4) Two of the several possible reasons for the nonlinear dependence are: (a) the observed merging of flamelets and (b) a geometric effect that is associated with Bunsen flames, which become shorter and have less distance to wrinkle as they propagate faster. Images of CH layers show merging events: thin fingers of flame where segments are propagating toward each other. Local flamelet extinction is not a realistic reason for the bending in this study, as extinction was not observed.

(5) In-plane components of the local stretch rate along fully turbulent premixed flames were measured; previously such measurements were obtained only for laminar or nonpremixed flames. The stretch efficiency function (Γ_K) was measured for Bunsen flames and is best fit by the empirical relation

$$\Gamma_K = C_1\left(\frac{\ell}{\delta_{L0}}\right)^2\left(\frac{\bar{U}}{S_{L0}}\right)^2.$$

This indicates that large eddies are more efficient at stretching the flame than small eddies, as was predicted by Meneveau and Poinsot. It also indicates that the mean velocity $\bar{U}$ is important and is believed to be because it affects the velocity component that is tangential to the wrinkled flame surface.

(6) CH-PLIF/PIV diagnostics were shown to be adequate to image eddy structure, eddy sizes, and certain pairs of eddies which were observed to exert positive and negative strain.

(7) The measured average thickness of the CH reaction layer flamelets does not change as turbulence intensity is increased by a factor of 5. Many pockets of reactants are seen. This indicates that conditions were within the "corrugated flamelet" regime. If distributed reaction zones exist, then the thickness of the CH regions would be expected to increase with turbulent diffusivity, which is proportional to u', and this was not observed to occur. The PLIF spatial resolution of 0.2 mm was less than the average CH layer thickness of 0.7 mm, but improved resolution is needed to better define flamelet properties.

Acknowledgments

This research was supported by National Science Foundation Grant CTS-9904198, monitored by Dr. Farley Fisher. Support to maintain the CH PLIF-PIV diagnostics was provided by the Air Force Office of Scientific Research.

Appendix A. Details of the diagnostics, the data reduction procedures, uncertainties, and boundary conditions

CH fluorescence was obtained by tuning the 390.30-nm, 15-mJ output of a Nd:YAG-pumped dye laser to the $Q_1(7.5)$ transition of the $B^2\Sigma^- - X^2\Pi$ ($v' = 0,\ v'' = 0$) band. Fluorescence was collected from the $A–X$ $(1,1)$, $(0,0)$ and $B–X$ $(0,1)$ bands at wavelengths from 420 to 440 nm. The array of the PIMAX camera was 170 × 170 pixels after 3 by 3 pixel binning. A Schott KV-418 color glass filter provided greater than six orders of magnitude of rejection at 390 nm while maintaining 90% transmission at 430 nm. It was imperative to reject scattering and emission from the 0.5-μm alumina PIV particles using BG-1 and KV-418 filters and a short intensifier gate width of 80 ns. Background emission was further reduced by gating the intensifier microchannel plate. The thicknesses of all three laser sheets were measured by translating a 25-μm slit across the beam at the probe region; sheet thickness is the distance between the locations where the photodiode signal was 25% of the peak value.

The PIV system included an interline transfer CCD camera with 2k × 2k resolution (Redlake ES-4.0) that was fitted with an interference filter (centered at 532 nm and with a 10-nm bandpass) and a Nikon 105-mm macro lens set to an f-stop of f/8. The PIV interrogation box was 16 × 16 pixels. An Epix, Inc., interface card and controlling software (XCAP) were used for capturing images. Typically, 4 sets of 50 images were collected for each condition; frames were recorded at 1-s intervals, a limitation imposed by the ES-4.0 camera. Accordingly, the PIV lasers were Q-switched at 1 Hz, while the flashlamps were triggered at 10 Hz. Timing for the lasers and cameras was controlled with a Quantum Composer 9318 delay generator, which allows subharmonic cuing and triggering. Commercial LaVision PIV software was applied that employs adaptive interrogation-region offsetting. Mie scattering diagnostics were used to visualize the boundary between product and reactants. The 532-nm Nd:YAG laser light that was scattered by micron-sized PD-23 oil drops was recorded with a high-resolution (3k × 2k) Kodak 460 digital camera. The resolution provided by each pixel was 60 μm.

The uncertainty in the global consumption speed ($\Delta\bar{S}_T$) was determined by taking the logarithmic derivative of Eq. (5c) to obtain

$$\Delta\bar{S}_T/\bar{S}_T = \left[(\Delta\dot{m}_R/\dot{m}_R)^2 + (\Delta\bar{A}_F/\bar{A}_F)^2\right]^{1/2}. \quad \text{(A.1)}$$

The mass flow rate measurement had an uncertainty ($\Delta\dot{m}_R/\dot{m}_R$) of 3% and the error in $\bar{A}_F$ was 5%, so Eq. (A.1) indicates that the error in determining consumption speed was 6%.

The component of the vorticity vector that is normal to the laser sheet (ω_z) is defined as $\partial v/\partial x - \partial u/\partial y$ and was measured using the following 8-point circulation method [46], which has second-order accuracy:

$$\begin{aligned}\omega_{i,j} = {} & \frac{\mathbf{u}_{i-1,j-1} + 2\mathbf{u}_{i,j-1} + \mathbf{u}_{i+1,j-1}}{8\Delta y} \\ & + \frac{\mathbf{v}_{i+1,j-1} + 2\mathbf{v}_{i+1,j} + \mathbf{v}_{i+1,j+1}}{8\Delta x} \\ & + \frac{\mathbf{u}_{i+1,j+1} + 2\mathbf{u}_{i,j+1} + \mathbf{u}_{i-1,j+1}}{8\Delta y} \\ & + \frac{\mathbf{v}_{i-1,j+1} + 2\mathbf{v}_{i-1,j} + \mathbf{v}_{i-1,j-1}}{8\Delta x}, \end{aligned} \quad \text{(A.2)}$$

where $\Delta x = \Delta y = 8$ pixels (0.14 mm), with 50% overlapping of 16-pixel interrogation regions (IRs). This method has less random error than a central difference formula, because it is equivalent to central differencing a velocity field smoothed with a 3 × 3 kernel [46]. Random errors in the vorticity measurements are due to (1) the error in determining the peak location of the PIV correlation function, (2) contributions from small-scale eddies that are not resolved, (3) thermophoretic velocity bias, (4) particle-image distortion from imaging through the flame, and (5) perspective distortion error. Error in determining the peak location will depend on the signal-to-noise ratio (SNR) of the "signal" peak in the correlation map and is often the dominant error. With a recursive algorithm, such as the one employed, IR shifting will retain the maximum number of particle pairs (and thus the SNR will be maximized), and the effective particle image shift should be $\leqslant 0.5$ pixel. With a numerical simulation, Raffel et al. [46] show the dependence of the peak-finding rms uncertainty, δ_{dis}, on particle-image shift for an IR size of 32 × 32 pixels, mean particle-image diameter of 2.2 pixels, 8-bits particle-image digitization, and various numbers of particle pairs. Applying the analysis of Raffel et al. to the present conditions, with an average of 5.2 particle pairs per IR, the rms uncertainty vs. particle image shift increases from $\delta_{dis} < 0.005$ pixel with no shift to about 0.04 pixel at 0.5 pixel image shift. It should be noted that in the cold reactants, the typical number of particles was much greater than 5 (and thus one would

expect lower δ_{dis}), whereas in the hot products, the number of particle pairs was $\leqslant 5$.

Using an estimated value of 0.5 pixel image shift, results [46] indicate that $\delta_{\text{dis}} = \pm 0.04$ pixel; with a typical particle displacement of 8 pixels, this yields a relative uncertainty of $\delta u/u = \delta_{\text{dis}}/8 \approx \pm 0.005$ in the velocity. Because random errors add in quadrature, the random uncertainty in the vorticity is

$$\delta\omega = \left(\sqrt{8 + 4 \cdot 2^2}/8\right) \cdot \delta_{\text{dis}}/(\Delta x \cdot \Delta t) \approx 0.6\delta_{\text{dis}}/(\Delta x \cdot \Delta t),$$

where Δt is the separation in time of the PIV pulses ($\Delta t = 40$ and 15 μs for cases 3 and 8, respectively). Thus, using these numbers, the uncertainties in vorticity are estimated to be 75 and 200 s^{-1} for cases 3 and 8, respectively; this represents the "noise floor" for measurement of vorticity. By using the 8-point circulation method, the spatial resolution of the vorticity measurement is 32 pixels on a side (0.55 mm) and ~ 0.3 mm thick. It is clear from the above equation the *amplification* effect of using smaller IRs on the derivative quantities (since Δx becomes smaller); the use of smaller IRs can also amplify the uncertainty of derivative quantities because of the reduction in the correlation SNR.

The total strain rate on the flame is given by Eq. (10a); the measured in-plane contribution is

$$K_{\text{s}} = \left(1 - n_x^2\right)\frac{\partial u}{\partial x} - n_x n_y\left(\frac{\partial u}{\partial y} + \frac{\partial v}{\partial x}\right) + \left(1 - n_y^2\right)\frac{\partial v}{\partial y}. \tag{A.3}$$

The velocity derivatives were determined from the second-order accurate differencing relation, which for the v derivative is

$$\frac{\partial v}{\partial y} = \frac{1}{6\Delta y}(\mathbf{v}_{i+1,j} - \mathbf{v}_{i-1,j} + \mathbf{v}_{i+1,j-1} - \mathbf{v}_{i-1,j-1} + \mathbf{v}_{i+1,j+1} - \mathbf{v}_{i-1,j+1}). \tag{A.4}$$

The spatial resolution of the strain measurement is the same as that of the vorticity measurement: $0.55 \times 0.55 \times 0.3$ mm^3. In order to measure the normal vector ($\mathbf{n}$) and the radius of curvature of the CH reaction layers, a third-order polynomial was fit through every five points (each point separated by 0.2 mm, the pixel resolution on the CH ICCD camera) along the isoline of maximum CH signal. At the center of these five points, the curvature ($1/R_{\text{c}}$) is given by

$$1/R_{\text{c}} = \nabla \cdot \mathbf{n} = \mathbf{T} \cdot (d\mathbf{n}/ds). \tag{A.5}$$

$\mathbf{T}$ is a unit vector that is tangential to the isoline of maximum CH signal, s is the coordinate along the CH isoline. If we simply assume that we can locate the CH countour peak within half a pixel at each camera pixel, then we might expect the error in the flame surface normal angle to be $\delta\varphi \approx \pm 0.1$ radian.

In addition to the errors sources noted for the derived vorticity, those contributing to error in the strain rate measurements are due to uncertainties in the surface normal and the out-of-plane velocity gradients. The random error contribution to one of the velocity derivatives, $\partial v/\partial y$, for example, from uncertainty in PIV peak finding is

$$\delta\frac{\partial v}{\partial y} = \sqrt{6}/6 \cdot \delta_{\text{dis}}/(\Delta y \cdot \Delta t) \approx 0.4\delta_{\text{dis}}/(\Delta y \cdot \Delta t),$$

equaling ~ 50 and 130 s^{-1} for cases 3 and 8, respectively. The sensitivity to uncertainty in the flame-surface normal, using the in-plane strain equation, is

$$\frac{\partial K_{\text{s}}}{\partial\varphi} = \left(\sin^2\varphi - \cos^2\varphi\right) \cdot \left(\frac{\partial u}{\partial y} + \frac{\partial v}{\partial x}\right) + 2\sin\varphi\cos\varphi \cdot \left(\frac{\partial u}{\partial x} - \frac{\partial v}{\partial y}\right).$$

Considering, for simplicity, a flame segment that is vertically oriented ($\varphi = 0$), yields

$$\delta K_{\text{s}} = \left[\left(\delta\varphi \cdot \left(\frac{\partial u}{\partial y} + \frac{\partial v}{\partial x}\right)\right)^2 + \left(\delta\frac{\partial v}{\partial y}\right)^2\right]^{1/2}.$$

Here, the random uncertainty has both a "floor" component (50 and 130 s^{-1}) and a component proportional to the velocity derivatives. If, say, $\left(\frac{\partial u}{\partial y} + \frac{\partial v}{\partial x}\right) =$ 300 and 1000 s^{-1}, then $\delta K_{\text{s}} \cong 60$ and 165 s^{-1}, yielding percentage random errors of 20 and 17%, for cases 3 and 8, respectively.

Other contributions (noted above) to the error include those from the small-scale eddies, thermophoretic velocity bias, flame-induced image distortion, and perspective imaging error (where out-of-plane particle displacements appear as in-plane displacements). Error is introduced by small-scale eddies because of the finite resolution of the PIV measurement: ~ 0.27 mm for velocities. In the reactants, 0.27 mm was less than 10 and 3% of the integral scales for cases 3 and 8, respectively. Relative to the Taylor and Kolmogorov scales, the PIV resolution is comparable to the Taylor scale (Table 2) and three to six times larger than the Kolmogorov scale. Wyngaard [47] integrated the area under the spectrum of scalar gradients and showed that if the resolution is three times the Kolmogorov scale, the resulting error in the gradient is 20%. This is the estimated error in the strain rate due to small scale eddies in the present work.

Thermophoresis is the tendency for a particle to drift "down" the temperature gradient. Sung et al. [48] found that the thermophoretic drift velocity, equaling

the difference between the gas velocity and the particle velocity, was ~ 0.1 m/s. If it is assumed that this bias error occurs over the flamefront thickness of ~ 0.7 mm, then the magnitude in the bias error in the velocity derivative normal to the flame surface can be reasonably large, $\sim 140\ \mathrm{s}^{-1}$. However, derivatives away from the flame surface or *along the flame surface* (as with flamefront strain) are minimally affected by thermophoresis since the temperature gradient is small. While deriving a contribution to the uncertainty (particularly random uncertainty) from flame-induced image distortion is difficult, we can more easily estimate the effect of perspective imaging error. If we assume that the out-of-plane velocity component is equal to the turbulence intensity and that $w' = v'$ (assuming isotropic turbulence), then at a 10-mm radius from the image center with the lens 240 mm from the object plane and a turbulence intensity of 20%, this will appear as an in-plane displacement of $\sim (8\ \text{pixels} \times 0.20) \times (10/240) = \pm 0.07$ pixel. Of course, for this error to contribute the random uncertainty in strain or vorticity, it would have to vary over a spatial scale, e.g., the characteristic eddy size. Only when the characteristic eddy size is less than 1 mm will perspective imaging error be a significant contributor to random uncertainty of the derivative quantities.

The out-of-plane contribution to the strain rate was not measured; it is the difference between Eqs. (10a) and (A.3), which is

$$K_{\mathrm{s,op}} = -\left(1 - n_z^2\right)(\partial w/\partial z) - n_z n_y(\partial w/\partial y + \partial v/\partial z) - n_z n_x(\partial w/\partial x + \partial u/\partial z). \quad \text{(A.6)}$$

This out-of-plane contribution is argued to be between 25 and 33% of the total strain rate. Each of the velocity derivatives in Eq. (A.6) is estimated to have an equal magnitude, on average, since grid-generated turbulence is nearly isotropic. If the normal to the flame sheet also is assumed to be oriented isotropically, then $n_x^2 = n_y^2 = n_z^2 = 1/3$, since the sum of n_x^2, n_y^2 and n_z^2 must add to unity, and the correlation terms such as $n_x n_y$ would be zero. Inserting these values into Eqs. (A.6) and (10a) provides an estimate of the out-of-plane strain rate that is one-third of the total strain rate. A more probable flame orientation is not isotropic, but is one that for which each segment of the flame is more likely to be inclined at about 45 degrees to the flow, as is the flame brush. For this orientation, n_x^2 and n_y^2 are equal (and each has a value of $1/2$) but n_z is nearly zero. The correlation $n_x n_y$ is 0.5 for this orientation. Inserting these values into Eqs. (A.6) and (10a) provides an estimate of the out-of-plane strain rate that is one-fourth of the total strain rate.

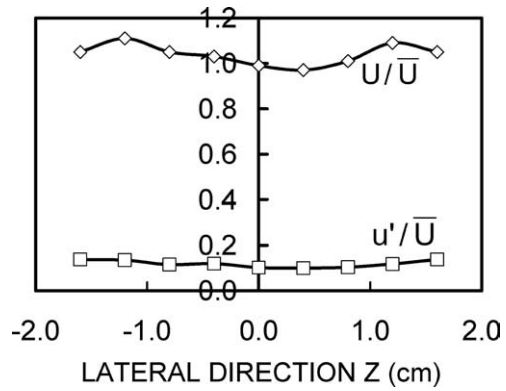

Fig. 16. Boundary conditions at burner exit ($x = 0$) indicating the degree of two-dimensionality in the mean flow properties. The z direction is perpendicular to the laser light sheet, as shown in Fig. 1. All data were obtained at $x = 0$, $y = 0$.

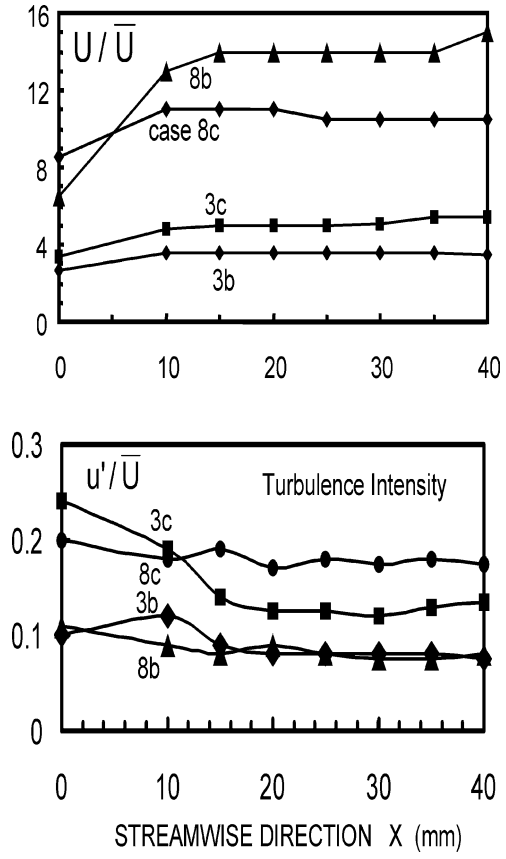

Fig. 17. Axial velocity and velocity fluctuations along the burner centerline ($y = 0$, $z = 0$) for four cases.

Error is introduced because small-scale eddies are not resolved by the spatial resolution of the PIV system, which was 0.3 mm. This dimension was less than 10% of the integral scale for case 3 and was

less than 3% of the integral scale for case 8. The Taylor scales $(\ell(u'\ell/\nu)^{-1/2})$ and the Kolmogorov scales $(\ell(u'\ell/\nu)^{-3/4})$ are listed in Table 1. The PIV spatial resolution was about equal to the Taylor scale and was three to six times the Kolmogorov scale. Wyngaard [47] integrated the area under the spectrum of scalar gradients and showed that if the resolution is three times the Kolmogorov scale, the resulting error in the gradient is 20%. This is the estimated error in the strain rate due to small eddies in the present work. Another potential source of uncertainty is thermophoresis, which is the tendency for a particle to drift down a temperature gradient. Sung et al. [48] found that the thermophoretic drift velocity (equaling the difference between the gas velocity and the particle velocity) was 0.1 to 0.15 m/s. If it is assumed that this error occurs over a distance of 2 mm (which would require a temperature gradient change of ~ 2000 K over this distance), then the error in the velocity derivative would be 50 to 75 s^{-1}.

Figs. 16 and 17 quantify the boundary conditions at the burner exit that are needed to numerically simulate the experiment. $U_{CL,0}$ and u' were measured with a laser velocimeter and normalized by $\bar{U}$, which is proportional to the measured mass flow rate. Fig. 16 indicates that the flame has 2D mean properties near $z = 0$, which is the laser sheet location, as the exit conditions deviate by no more than 10% over a 2-cm distance in the z direction.

References

[1] J.B. Bell, M.S. Day, J.F. Grcar, Proc. Combust. Inst. 29 (2002) 1987–1993.
[2] R.O.S. Prasad, J.P. Gore, Combust. Flame 116 (1999) 1–14.
[3] D. Veynante, J.M. Duclos, J. Piana, Proc. Combust. Inst. 25 (1994) 245–250.
[4] T.A. Baritaud, J.M. Duclos, A. Fusco, Proc. Combust. Inst. 26 (1996) 2627–2633.
[5] J.M. Duclos, D. Veynante, T. Poinsot, Combust. Flame 95 (1993) 101–121.
[6] F. Charlette, C. Meneveau, D. Veynante, Combust. Flame 131 (2002) 159–180.
[7] E.R. Hawkes, R.S. Cant, Combust. Flame 126 (2001) 1617–1629.
[8] R. Knikker, D. Veynante, C. Meneveau, Proc. Combust. Inst. 29 (2002) 2105–2110.
[9] H.G. Weller, G. Tabor, A.D. Gosman, C. Fureby, Proc. Combust. Inst. 27 (1998) 899–904.
[10] K.N.C. Bray, Proc. R. Soc. London A 431 (1990) 313–323.
[11] S.M. Candel, T.J. Poinsot, Combust. Sci. Technol. 70 (1990) 1–15.
[12] C. Meneveau, T. Poinsot, Combust. Flame 86 (1991) 311–325.
[13] G. Damkohler, Z. Electrochem. 46 (1940) 601.
[14] B. Lewis, G. von Elbe, Combustion, Flames and Explosions of Gases, second ed., Academic Press, New York, 1961.
[15] K.N.C. Bray, R.S. Cant, Proc. R. Soc. London A 434 (1991) 217–227.
[16] R.K. Cheng, I.G. Shepherd, Combust. Flame 85 (1991) 7–26.
[17] D.A. Knaus, F.C. Gouldin, Proc. Combust. Inst. 28 (2000) 367–373.
[18] M.-S. Wu, S. Kwon, J.F. Driscoll, G.M. Faeth, Combust. Sci. Technol. 73 (1990) 327–350.
[19] J.H. Bechtel, R.J. Blint, C.J. Dasch, D.A. Weinberger, Combust. Flame 42 (1981) 197–213.
[20] M.I. Hassan, K.T. Aung, G.M. Faeth, Combust. Flame 115 (1998) 539–550.
[21] C.D. Carter, J.M. Donbar, J.F. Driscoll, Appl. Phys. B 66 (1998) 129–131.
[22] J.M. Donbar, J.F. Driscoll, C.D. Carter, Combust. Flame 125 (2001) 1239–1257.
[23] A. Ratner, J.F. Driscoll, J.M. Donbar, C.D. Carter, J.A. Mullin, Proc. Combust. Inst. 28 (2000) 245–250.
[24] R.K. Cheng, T.T. Ng, Combust. Flame 57 (1984) 155–167.
[25] I.G. Shepherd, R.K. Cheng, Combust. Flame 127 (2001) 2066–2075.
[26] C. Ghenai, F.C. Gouldin, I. Golkalp, Proc. Combust. Inst. 27 (1998) 979–984.
[27] H. Kobayashi, K. Seyama, H. Hagiwara, Y. Ogami, Proc. Combust. Inst. 30 (2005), in press.
[28] D. Bradley, Proc. Combust. Inst. 24 (1992) 247–253.
[29] R.G. Abdel-Gayed, D. Bradley, M. Lawes, Proc. R. Soc. London A 414 (1987) 389–413.
[30] S.S. Shy, W.J. Lin, K.Z. Peng, Proc. Combust. Inst. 28 (2000) 561–566.
[31] E. Bourguignon, L.W. Kostiuk, Y. Michou, I. Gokalp, Proc. Combust. Inst. 26 (1996) 447–452.
[32] V. Karpov, A. Lipatnikov, V. Zimont, Proc. Combust. Inst. 26 (1996) 249–254.
[33] N. Peters, J. Fluid Mech. 348 (1999) 107–140.
[34] R.C. Aldredge, Combust. Flame 90 (1992) 121–133.
[35] B. Denet, Combust. Theory Model. 3 (1999) 585–595.
[36] H. Beretycki, G.I. Sivashinsky, SIAM J. Appl. Math. 51 (2) (1991) 344–354.
[37] J.H. Chen, T. Echekki, W. Kollmann, Combust. Flame 116 (1999) 15–48.
[38] C.J. Mueller, J.F. Driscoll, D.L. Reuss, M.C. Drake, M.E. Rosalik, Combust. Flame 112 (1998) 342–358.
[39] J.O. Sinibaldi, J.F. Driscoll, C.J. Mueller, J.M. Donbar, C.D. Carter, Combust. Flame 133 (2003) 323–334.
[40] H.N. Najm, P.S. Wyckoff, Combust. Flame 110 (1997) 92–112.
[41] C.K. Law, D.L. Zhu, G. Yu, Proc. Combust. Inst. 21 (1986) 1419–1426.
[42] F. Dinkelacker, A. Soika, D. Hofmann, A. Leipertz, W. Polifke, K. Dobbeling, Proc. Combust. Inst. 27 (1998) 857–865.
[43] I.G. Shepherd, R.K. Cheng, T. Plessing, C. Kortschik, N. Peters, Proc. Combust. Inst. 29 (2002) 1833–1838.
[44] M. Tanahashi, Y. Nada, Y. Ito, T. Miyauchi, Proc. Combust. Inst. 29 (2002) 2041–2049.
[45] I.G. Shepherd, W.T. Ashurst, Proc. Combust. Inst. 24 (1992) 485–491.

[46] M. Raffel, C. Willert, J. Kompenhans, Particle Image Velocimetry: A Practical Guide, Springer-Verlag, Heidelberg.
[47] J.C. Wyngaard, Phys. Fluids 14 (1971) 1821–1830.
[48] C.J. Sung, C.K. Law, R.L. Axelbaum, Combust. Sci. Technol. 99 (1994) 119–129.